Sulfur Distribution Analysis in Lithium–Sulfur Cathode via Confined Inverse Vulcanization in Carbon Frameworks

Bijian Deng, Frieder Scheiba,* Anhao Zuo, Sylvio Indris, Hang Li, Hannes Radinger, Alexander Grimm, and Christian Njel

Lithium–Sulfur (Li–S) batteries are promising energy storage devices due to their high theoretical energy density. However, challenges such as the shuttling effect and volume expansion have significantly hindered their cycle life and capacity retention. Furthermore, the complex kinetic pathways in Li–S batteries call for advanced characterization techniques to unravel underlying mechanisms. In this study, a hollow porous carbon (HPC) is used as a microreactor, where inverse vulcanization occurs between 1,3-diisopropylbenzene (DIB) and sulfur (S_8), resulting in the creation of three-dimensionally interconnected and well-distributed S-DIB in carbon frameworks. As a result, the dual confinement strategy imparts Li–S coin cells with remarkable cycling stability and capacity retention, exhibiting an impressive capacity of 866 mAh g^{-1} when returning to 0.1 C after 100 cycles of rate capability tests. Particularly, the Energy-selective Backscattered (EsB) assisted Scanning Electron Microscope (SEM) technique as a novel approach is introduced to distinguish different lengths of polysulfides. Their distribution is visualized in the cross-section view of the electrode in a micrometer range. These EsB images provide concrete indications of the sulfur evolution process and explain the capacity degradation during cycling.

1. Introduction

Lithium–Sulfur (Li–S) batteries are highly competitive for next-generation energy storage due to their high-energy density and sulfur's natural abundance.[1,2] However, their commercial viability is hindered by challenges like the shuttle effect, volume changes during de/lithiation, and the insulating nature of S_8 and Li_2S/Li_2S_2. Recent studies have shown that copolymerizing elemental sulfur with organic linkers, such as 1,3-diisopropenylbenzene,[3,4] trithiocyanuric acid,[5] and tetra(allyloxy)-1,4-benzoquinone,[6] can suppress the shuttle effect. To address the conductivity issue of poly-S, S-DIB has been combined with conductive carbon materials.[3,7–9] Additionally, on the technical side, the fabrication of S-DIB with graphene oxide through 3D printing has also been reported to achieve a well-distributed architecture within conductive frameworks.[10] This innovative combination enhances the utilization of sulfur copolymers and effectively mitigates the volume change experienced during cycling. Meanwhile, carbon materials derived from metal-organic frameworks demonstrate remarkable porosity and excellent conductivity.[11] This positions them as highly promising micro-reactors for facilitating the processing of the inverse vulcanization, thus preparing the uniform poly-S/carbon structure in one pot and potentially solving the issues mentioned above.

Understanding the complex redox processes in Li–S batteries is crucial for unlocking their full potential.[12] High-resolution imaging techniques, such as X-ray Tomographic Microscopy,[13,14] X-ray Absorption Spectroscopy,[15,16] and confocal Raman Spectroscopy,[17,18] have been developed to reveal underlying mechanisms. For instance, Abruña's group used *operando* confocal Raman microscopy to investigate and quantify Li–S redox processes, developing a kinetics model.[18] These techniques mostly rely on the identification of reactants by mapping signal peaks in spectral data to image their distribution. This typically leads to images with low spatial resolution, which are time consuming to record or require synchrotron radiation facilities.

SEM is widely used in Li–S systems to provide microstructure insights, such as Li stripping/plating and Li_2S deposition.[19,20] However, ordinary secondary electron (SE) detectors are

B. Deng, F. Scheiba, A. Zuo, S. Indris, H. Li
Institute for Applied Materials (IAM)
Karlsruhe Institute of Technology (KIT)
Herrmann-von-Helmholtz-Platz 1, 76344 Eggenstein-Leopoldshafen, Germany
E-mail: frieder.scheiba@kit.edu
H. Radinger
Siemens AG
Schuckertstr. 2, 91058 Erlangen, Germany
A. Grimm
Institute for Biological Interfaces III (IBG-3)
Karlsruhe Institute of Technology (KIT)
Herrmann-von-Helmholtz-Platz 1, 76344 Eggenstein-Leopoldshafen, Germany
C. Njel
University of Versailles Saint-Quentin-en-Yvelines
55 avenue de Paris, Versailles 78000, France

ADVANCED
SCIENCE NEWS

www.advancedsciencenews.com

ADVANCED
ENERGY
MATERIALS

www.advenergymat.de

inadequate for low-conductivity materials like S/Li$_2$S. Recently, energy-selective backscattered electron imaging (EsB) has been applied to enhance contrast of low electron density materials, particularly at low voltages.[21–23] Heiner Jaksch discovered that exposing gold to a chlorine solution created a contrast detectable by the EsB detector.[24] This finding highlights the method's high surface sensitivity, attributed to the low electron energy of both primary and backscattered electrons. This sensitivity allows for the detection of chlorine ions forming a monolayer on gold, effectively masking the particles beneath. The combination of low interaction volume and the ability to distinguish different chemical environments of the same element makes the EsB imaging technique promising for obtaining high-resolution images of the spatial distribution of sulfur and lithiated sulfur.

In this study, we utilized a hollow porous carbon structure (HPC) to serve as a micro-reactor for inverse vulcanization. This strategy enabled simultaneous copolymerization and distribution of S-DIB, resulting in an electrode with stable cycling performance of 488 mAh g^{-1} after 500 cycles at 1C. Even at low electrolyte-to-sulfur ratios of 8 µL mg^{-1}, the electrode maintained 80% of its capacity after 200 cycles. EsB imaging was used to discriminate different lithium polysulfides and directly image their distribution in electrode cross-sections prepared by broad-ion beam polishing. This allowed a thorough investigation of the relationship between nanostructure evolution, active material loss and impedance change during the cycling process.

2. Results and Discussion

Inverse vulcanization is widely used to create sulfur-rich polymers, modifying sulfur into processable copolymers with adjustable thermomechanical properties. The inverse vulcanization was carried out in a HPC structure derived from ZIF-8, which served as a microreactor as shown in **Figure 1**a. In short, HPC was infused by sulfur and then polymerized with DIB to obtain a S-DIB@HPC composite. This approach aimed to simultaneously form and distribute S-DIB in a porous carbon matrix, maximizing the retention of DIB and intermediates.

To verify the feasibility of inverse vulcanization in HPC, we measured the differential scanning calorimetry (DSC) profiles of S@HPC, S-DIB, and S-DIB@HPC under air (Figure 1b). S@HPC displayed two sharp melting peaks at 121.4 and 105.6 °C, corresponding to orthorhombic and monoclinic sulfur phases. In contrast, the sulfur melting peaks in S-DIB@HPC and S-DIB were significantly reduced, indicating the conversion of crystalline sulfur to S-DIB with a glass transition temperature at −13.9 °C (Figure S1a, Supporting Information). The DSC profiles confirm that S$_8$ was almost entirely converted into S-DIB during copolymerization,[4] further verified by the disappearance of reflections from crystalline sulfur in XRD (Figure S1b, Supporting Information). Thermogravimetric analysis (TGA) showed sulfur loadings of 86 wt% for S-DIB, 70 wt% for S@HPC, and 69 wt% for S-DIB@HPC (Figure 1c), verifying that S-DIB was formed inside the porous carbon structure without sulfur loss.

To examine the internal pore structure and S-DIB distribution, we analyzed an ion-polished electrode using SEM. The cross-sectional view of HPC in Figure 1d and the magnification in Figure S2a (Supporting Information) reveal numerous individual hexagonal structures with internal pores. These structures

are densely packed in shell-like formations, providing space for inverse vulcanization and even distribution of the final product (S-DIB). The hollow structure was confirmed by TEM (Figure S2b, Supporting Information). Nitrogen adsorption/desorption isotherms (Figure S2c, Supporting Information) were recorded to determine the porosity and BET surface, resulting in a surface area of 706.4 m^2 g^{-1} and a total pore volume of 0.58 cm^3 g^{-1}. Comparison of tannic acid-etched and unetched ZIF-8-derived carbons show that mesopores are generated by the etching process. Pore size distributions evaluated by Horvath Kawazoe (Figure S2d, Supporting Information) and Barrett—Joyner–Halenda (Figure S2e, Supporting Information) methods show that HPC contains primarily micropores (0.6 nm) and mesopores (4.1 nm). Most carbon pores were filled with S-DIB after inverse vulcanization (Figure 1e). Energy dispersive X-ray spectroscopy (EDX) elemental mapping (Figure S3, Supporting Information) confirmed the uniform distribution of S-DIB across the HPC.

To evaluate the effects of confined inverse vulcanization on Li–S battery performance, we conducted galvanostatic charge-discharge tests at various C-rates (1C = 1675 mA g^{-1}). The S-DIB@HPC electrode shows superior rate capability compared to S@HPC and S-DIB, achieving 1091, 846, 771, 698, 583, 529, and 150 mAh g^{-1} at C-rates of 0.1, 0.2, 0.5, 1, 2, 3, and 5 C, respectively. The capacity is nearly fully retained when the current density is reset from 5C to 0.1C. The voltage difference (ΔE = 128 mV) calculated from the charge/discharge plateau (Figure S4, Supporting Information) indicates a lower electrochemical polarization for S-DIB@HPC compared to 163 and 140 mV for S@HPC and S-DIB, respectively, supporting rapid conversion of soluble lithium polysulfides (LiPS) to insoluble Li$_2$S$_2$/Li$_2$S.[25] At higher currents (3C), S-DIB@HPC shows increased polarization due to slow Li$_2$S precipitation, while S@HPC and S-DIB failed to convert Li$_2$S$_4$ to Li$_2$S$_2$/Li$_2$S, leading to a sharp capacity drop.

The change in ohmic resistance during charge and discharge was evaluated by galvanostatic intermittent titration technique (GITT) measurements at 0.05 C.[26,27] As is shown in **Figures 2**b and S5 (Supporting Information), S-DIB and S-DIB@HPC electrodes have smaller ΔR values during Li$_2$S nucleation than S@HPC, with S-DIB@HPC showing the lowest resistance during Li$_2$S activation. The results imply that polymerized sulfur domains enhance the nucleation kinetics in the Li$_2$S formation, and a favorable distribution in HPC can further improve the redox reaction rate. To further study the kinetic effects of the carbon structure on the S-DIB conversion process, cyclic voltammetry measurements at different sweep rates were conducted (Figure 2c; Figure S6, Supporting Information). All samples exhibit two broad overlapping cathodic and two anodic peaks. The cathodic peak at 2.31 V (C1) and anodic peak at 2.36 V (A1) correspond to the transformation between S-DIB and LiPS, while the cathodic peak at 2.08 V (C2) and anodic peak at 2.29 V (A2) correspond to the transformation between soluble LiPS and insoluble Li$_2$S$_2$ or Li$_2$S. The cathodic and anodic peak currents showed a linear relationship with the square root of the scanning rate, as described by the Randles–Sevcik equation. According to this equation, the slope of the curve ($I_p/v^{0.5}$) correlates to the apparent diffusion coefficient of the reacting species.[6,28] However, the Randles–Sevcik equation was originally derived for semi-infinite diffusion conditions, while diffusion in the HPC structure is strongly confined within its pores. Therefore, slopes
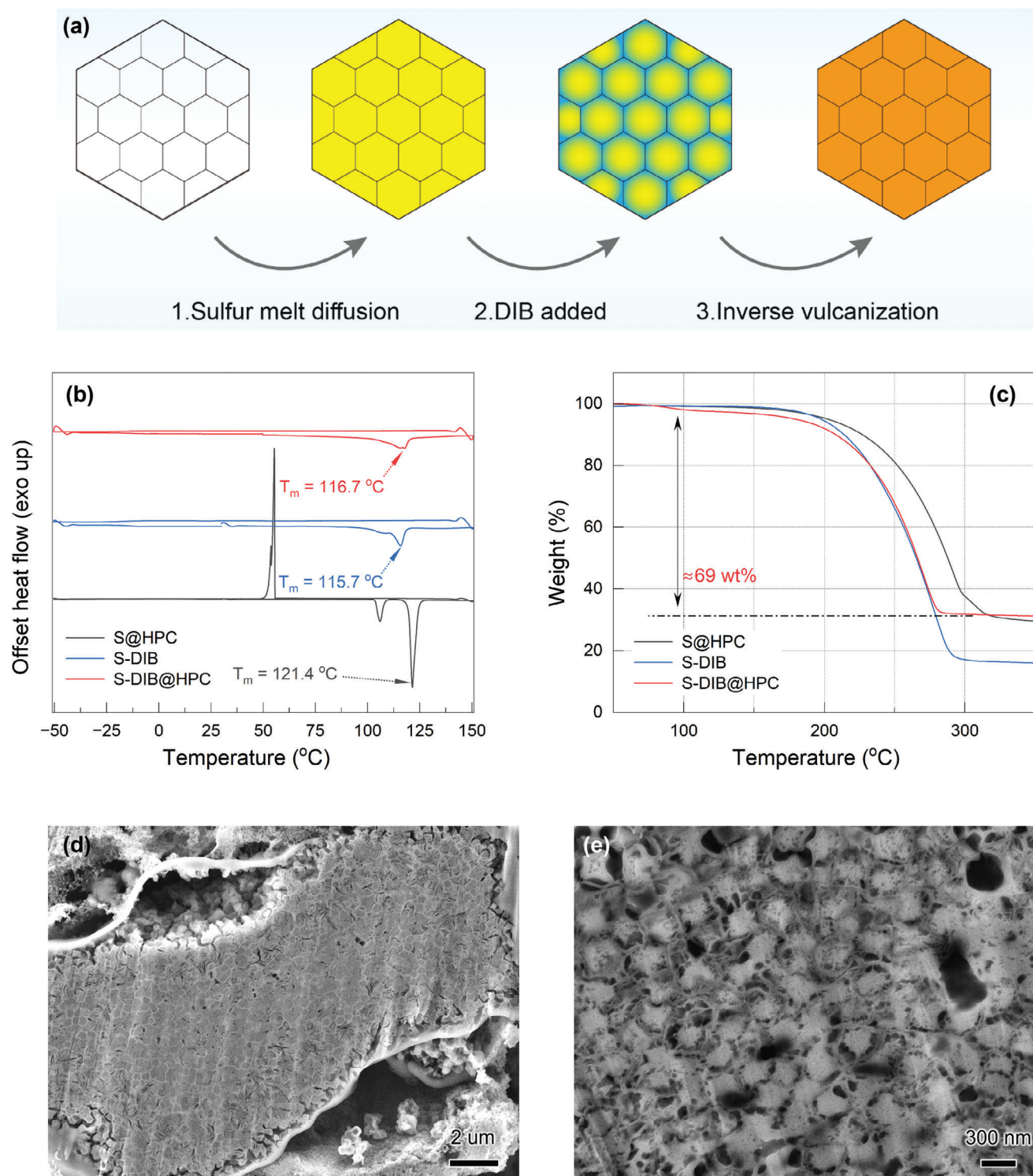
**ADVANCED
SCIENCE NEWS**

www.advancedsciencenews.com

**ADVANCED
ENERGY
MATERIALS**

www.advenergymat.de

Figure 1. a) Scheme of the inverse vulcanization process in HPC. In this scheme, "yellow" represents sulfur, "blue" DIB, and "orange" S-DIB. (b) DSC thermograms of S@HPC, S-DIB, and S-DIB@HPC. c) TGA profiles of S@HPC, S-DIB, and S-DIB@HPC. d) Cross-section SEM image of HPC. e) Cross-section SEM image of S-DIB@HPC.
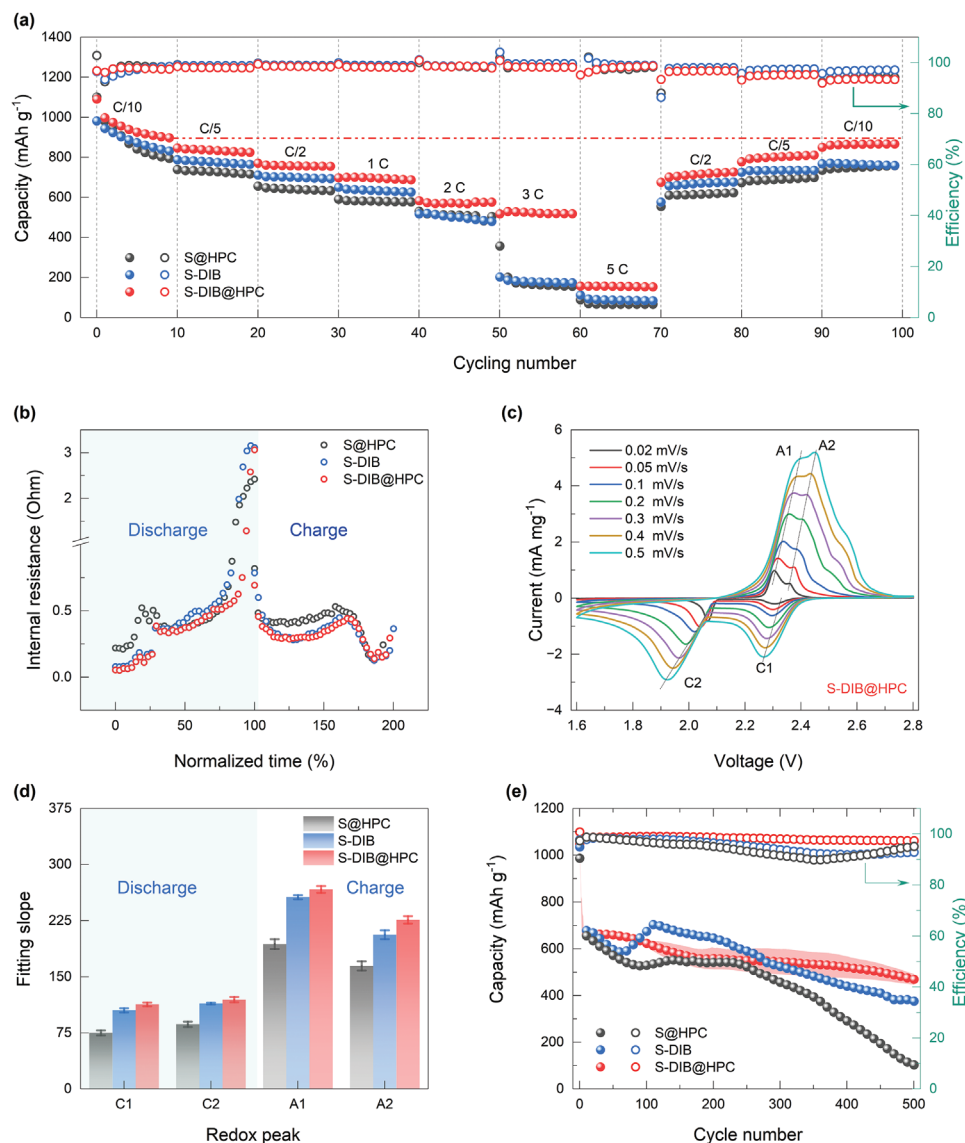
**ADVANCED
SCIENCE NEWS**

www.advancedsciencenews.com

**ADVANCED
ENERGY
MATERIALS**

www.advenergymat.de

Figure 2. Battery performance of S@HPC, S-DIB, S-DIB@HPC a) Rate measurements from 0.1 to 5 C. b) Internal resistance calculated from GITT. c) CV profiles of S-DIB@HPC d) The current versus square root of the scan rate measured from CV with various scan rates. e) Long cycling tests at 1C over 500 cycles.

obtained from Randles–Sevcik equation should not be interpretated as true diffusion coefficients, but rather as a kinetic parameter describing the S-DIB conversion process. The fitting results in Figure 2d show a higher slope for S-DIB@HPC, indicating a faster redox process of S-DIB confined in the HPC pore structure.

Benefiting from dual confinement by porous carbon and DIB, the S-DIB@HPC electrode achieves a reversible capacity of ≈488 mAh g⁻¹ after 500 cycles at 1C (Figure 2e), compared to ≈375 and ≈102 mAh g⁻¹ for S@HPC and S-DIB. Using a lean electrolyte loading of 8 µl mg⁻¹ of sulfur, the cell with a regular loading mass (1.6 mg S cm⁻²) maintained 80% capacity after 200 cycles at 1C (Figure S7a, Supporting Information). The cell with a higher loading mass of 4.5 mg S cm⁻² can provide a capacity as high as 851 mAh g⁻¹ after the activation of S-DIB and

can maintain 560 mAh g⁻¹ after 150 cycles (Figure S7b, Supporting Information). These results confirm that S-DIB confined in a hollow carbon matrix can improve the conversion of sulfur and minimize the "shuttle effect".

To better understand how the porous carbon structure affects the reaction kinetics and processes of S-DIB, we visualized the conversion process inside the material using broad ion beam cross-sectioning and EsB imaging in an electron microscope. In SEM, secondary electrons are typically used to examine a sample's topography, while back-scattered electrons (BSE) can reveal the distribution of elements based on atomic number (Z). However, classical BSE imaging is limited to high Z elements. An EsB detector enables to filter low energy (≈100–1500 eV) BSE, improving visualization of compounds consisting of light elements (**Figure 3a**).[29] Hence, we applied this detector in this study to

ADVANCED
SCIENCE NEWS
www.advancedsciencenews.com

**ADVANCED
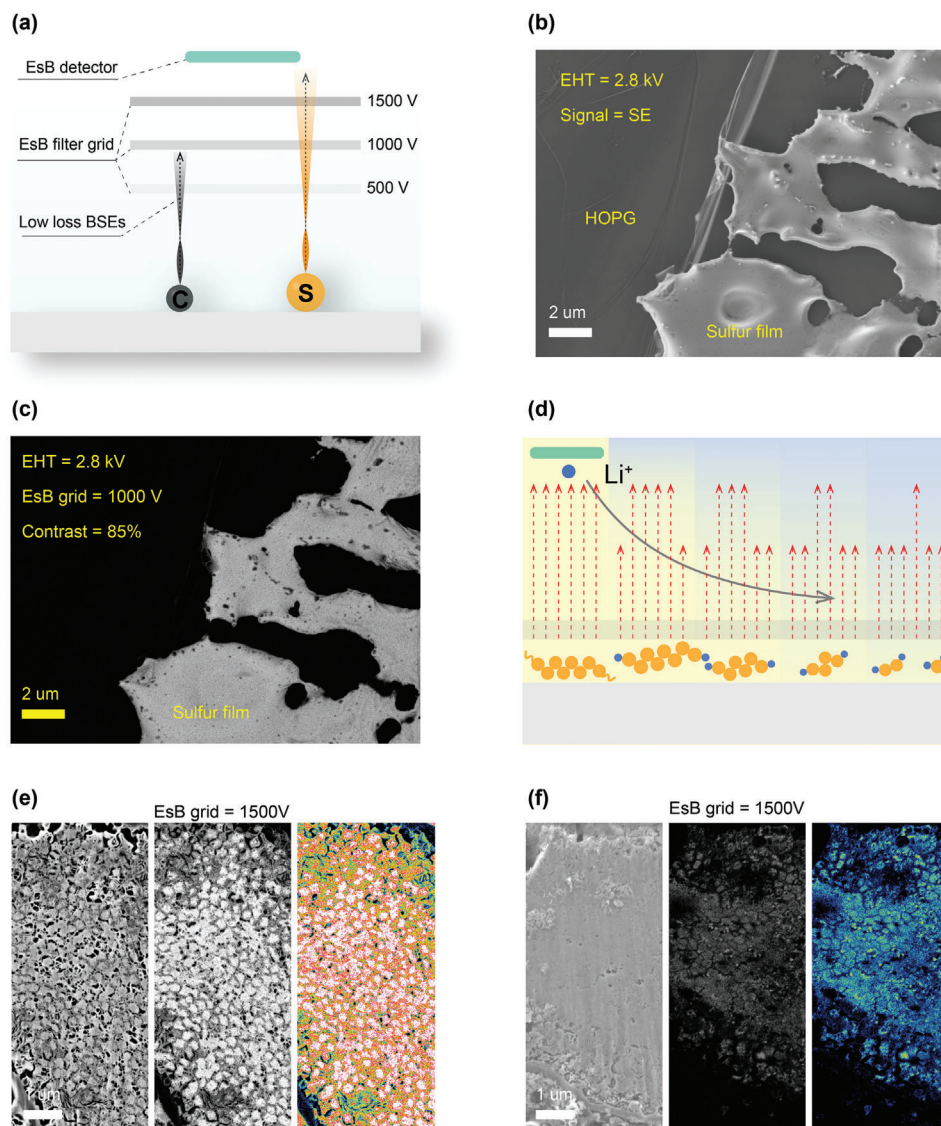ENERGY
MATERIALS**
www.advenergymat.de

Figure 3. a) Working mechanism of the EsB detector. b) SE image of deposited sulfur film on an HOPG substrate. c) Corresponding EsB image of deposited sulfur film on an HOPG substrate, EsB grid 1000 V. d) Scheme showing the decrease of backscattered electrons for sulfur species with increasing lithium content. Cross-section view of e) Pristine S-DIB@HPC electrode f) fully discharged S-DIB@HPC electrode, left: SE image, middle: EsB image, right: heat map processed EsB images.

investigate the multi-step phase transitions and reaction kinetics in Li–S batteries.

In sulfur battery, Li$^+$ migrates to the cathode during discharge, combining with sulfur to form Li$_2$S$_n$ and eventually Li$_2$S.[30] To determine the best EsB settings to detect sulfur and lithiated forms of sulfur, one half of a highly oriented pyrolytic graphite (HOPG) substrate was coated with sulfur, while the other half was freshly cleaved to serve as a carbon reference. Figure 3b shows a smooth HOPG surface on the left and a thin sulfur film on the right. Switching to the EsB detector (Figure 3c), elastic electrons from carbon are cut off, making the carbon region appear black, while higher energy BSE from sulfur pass the grid threshold, making the sulfur region appear brighter. With increasing lithiation depth, more Li$^+$ bonds with sulfur, causing regional contrast differences (Figure 3d). The higher

the level of lithiation the less electrons with the right threshold energy will be scattered back to the detector. Commercial sulfur and lithium sulfide powders were characterized using the EsB detector for validation. Figure S8 (Supporting Information) shows Li$_2$S particles appear darker than sulfur due to lower sulfur density and bonding state in Li$_2$S. Similar contrast differences can be observed in cross-sections of polished pristine and fully discharged electrodes characterized by SE and EsB detectors (Figure 3e,f; Figure S9, Supporting Information). SE images in Figure 3e,f show densely packed carbon with S-DIB and Li$_2$S$_2$/Li$_2$S, while the EsB images of the discharged electrode appear significantly darker. Thus, it is reasonable to expect that intermediates formed during discharge/charge exhibit brightness differences between sulfur and lithium sulfide.
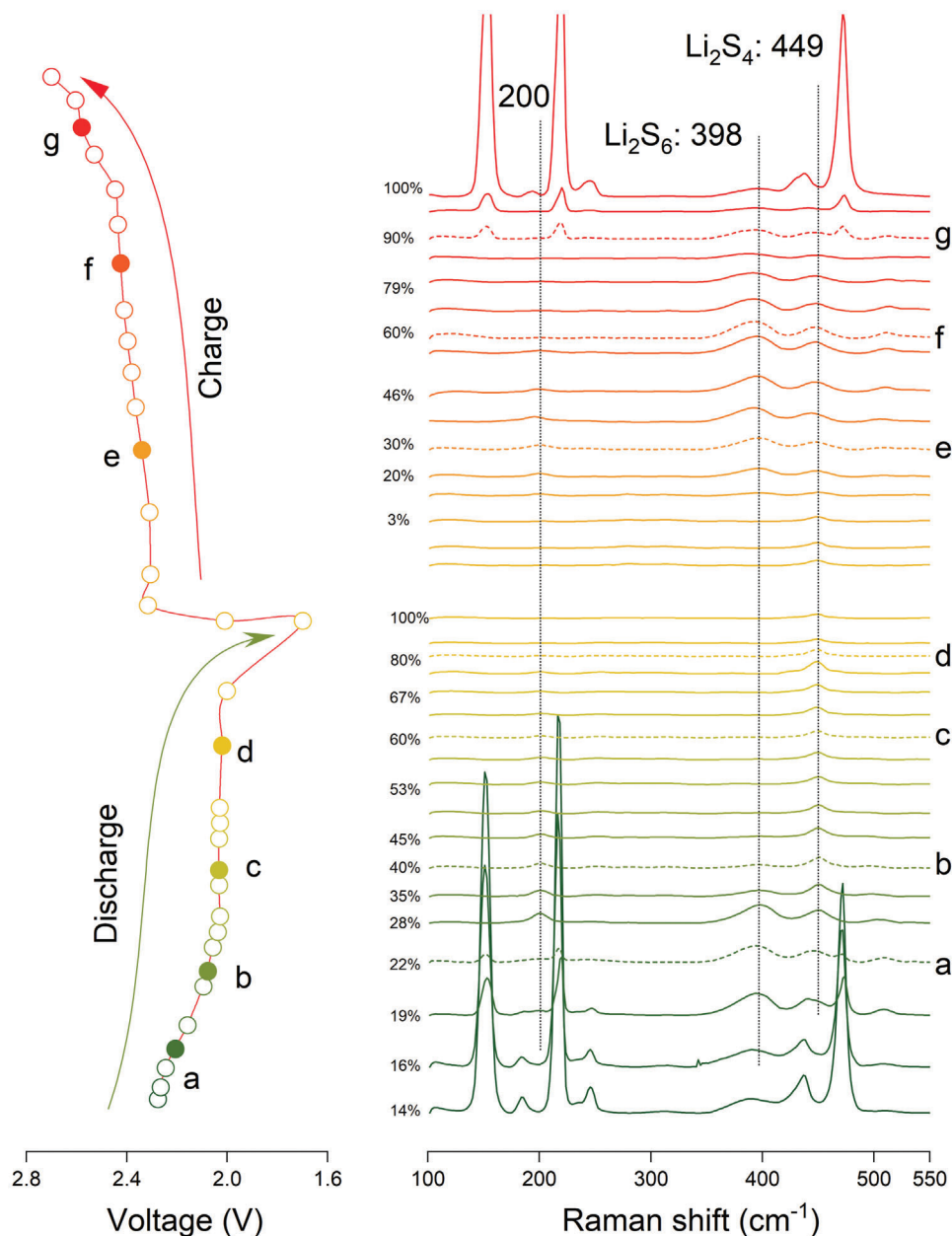
Figure 4. *Operando* Raman spectra.

However, there are certain imitations to this method. Phase mixtures of high-contrast and low-contrast materials may result in similar gray levels as a single-phase material with intermediate contrast. Additionally, a loss of sulfur can lead to a similar decrease in signal intensity as stepwise lithiation. Therefore, care must be taken when interpreting EsB images, and results should be confirmed by alternative methods. In this study, we use Raman and XPS to confirm if contrast changes are due to changes in sulfur concentration inside the electrode and if the lithium-sulfur compounds suggested by the gray level information from the EsB images are indeed present.

To understand the redox process of S-DIB and confirm the composition of each ion-polished electrode at different depths

of discharge (DOD) and states of charge (SOC), *operando* Raman spectroscopy experiments were conducted. **Figure 4** shows Raman spectra of an S-DIB@HPC electrode at different charge levels. At 14% DOD, the spectrum shows intense S–S stretching vibrations at 152, 217, and 473 cm^{-1}, with shoulder peaks at 246 and 438 cm^{-1} from S-DIB and long-chain polysulfides C(Li)-$S_x (x \approx 8)$-Li, similar to elemental sulfur (S8).[18,31] The peak at 400 cm^{-1} can be attributed to medium-chain LiPS, C(Li)-$S_x (x \approx 6)$-Li, while peaks at 200 and 449 cm^{-1} correspond to short-chain LiPS, C(Li)-$S_x (x \approx 4)$-Li.[18,31]

Electrodes at 20%, 40%, 60%, and 80% DOD, as well as 30%, 60%, and 90% SOC, were selected for further cross-sectional analysis by EsB imaging (**Figure 5**). The corresponding SE
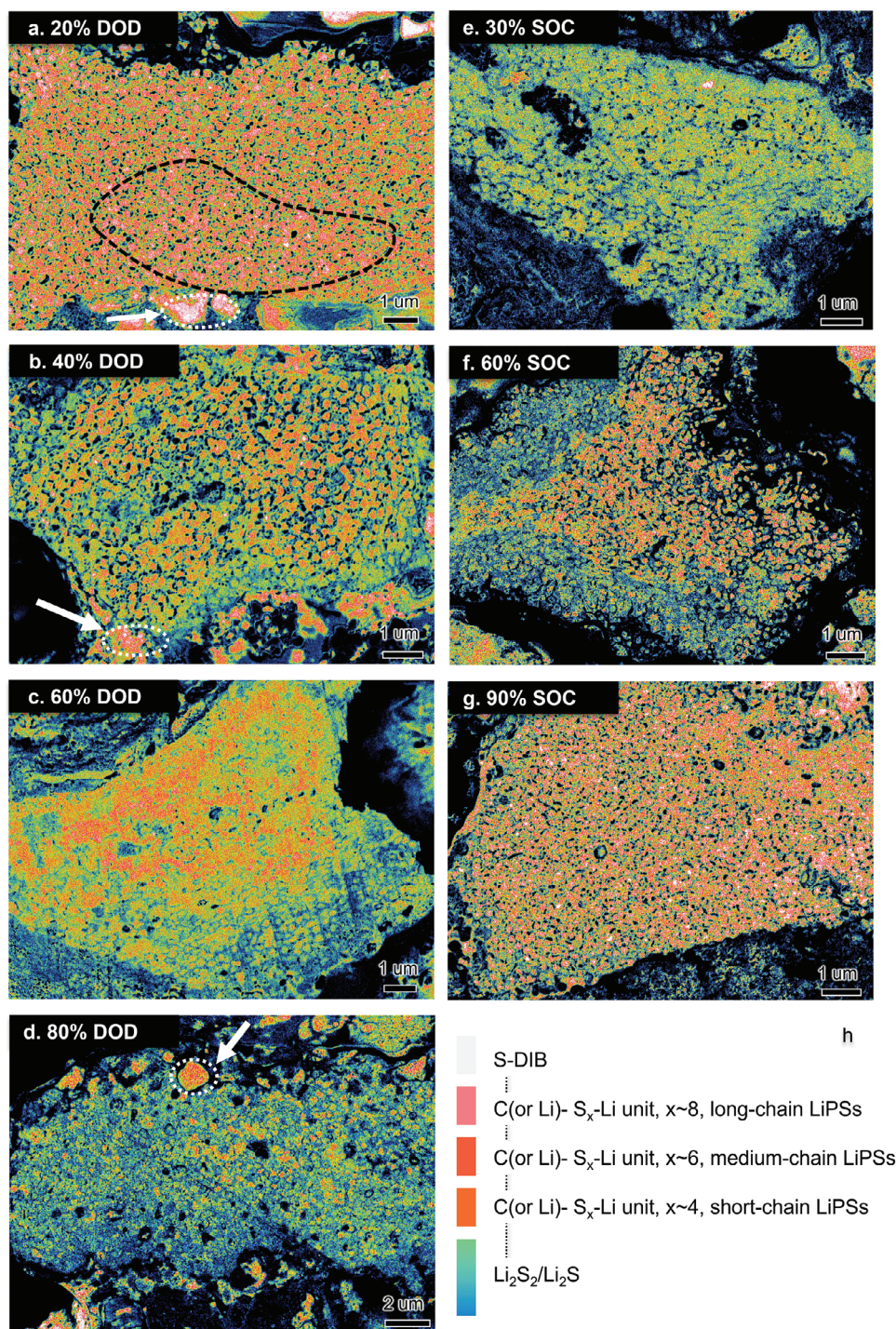
Figure 5. Heat map processed EsB image at a) 20 DOD, b) 40 DOD, c) 60 DOD, d) 80 DOD, e) 30 SOC, f) 60 SOC, g) 90 SOC, and h) color gradient and its corresponding species.

images are in Figure S10 (Supporting Information). EsB images were converted into heat-maps to visualize ion-insertion during lithiation. Bright pixels correspond to white and red, while dark pixels are blue and black. As the EsB signal intensity decreases with increasing lithiation, different colors represent changes between S-DIB and fully discharged S-DIB, indicating the transi-

tion from long-chain to medium-chain and short-chain organic and inorganic LiPS (Figure 5h). Combining Raman spectra and EsB images provides deeper insight into the lithiation and delithiation process during discharge and charge:

Galvanostatic discharge process: The S-DIB in HPC typically has one 1,3-diisopropylbenzene (DIB) unit per 44 linearly

**ADVANCED
SCIENCE NEWS**

www.advancedsciencenews.com

**ADVANCED
ENERGY
MATERIALS**

www.advenergymat.de

connected sulfur units.[32] At the beginning of discharge, fading Raman peaks of S-DIB show rapid consumption and conversion to Li_2S_8 and long-chained organosulfur-DIB units C-S_x-Li ($x\approx8$). At $\approx22\%$ DOD, the long-chain polysulfide peaks disappear, and new signals of C-(Li)-Sx-Li ($x\approx6$) emerge. Consistently, the EsB image at 20% DOD shows a small amount of long-chain C(Li)-Sx-Li ($x\approx8$) in the region marked by the dotted line, which is surrounded by medium-chain LiPS (Figure 5a; Figure S11, Supporting Information). Thus, during the initial 20% of discharge, polymeric S-DIB breaks down into long- and medium-chain LiPS, as described by reactions (1), (2), and (3).

As the discharge progresses, the peak of short-chain LiPS species increases, reaching its maximum at 35% DOD, while medium-chain LiPS gradually disappear. Thus, from 22% DOD to 35% DOD, the conversion of medium-chain LiPS to short-chain LiPS mainly takes place, which ends at 35 to 40% DOD, followed by the consecutive reduction of short-chain LiPS to Li_2S_2/Li_2S. The EsB image at 40% DOD (Figure 5b; Figure S12, Supporting Information) shows Li_2S_2/Li_2S (blue and green color) forming near the HPC particle surface, indicating that the conversion is limited by Li-diffusion or poor electronic conductivity of sulfur. The existence of Li_2S/Li_2S_2 toward the end of discharge was further confirmed by ^7Li NMR (Figure S13, Supporting Information).[28,33] Driven by the discharge current and the Li^+ concentration gradient, short-chain polysulfides progressively occupy less area at 60 and 80% DOD shown in Figure 5c,d and Figures S14 and S15 (Supporting Information). The parts of S-DIB formed outside the carbon skeleton are converted more slowly and cannot be completely lithiated due to their size, as shown by the white arrows in Figure 5a,b,d. S-DIB distributed in the carbon skeleton, on the other hand, can be lithiated evenly, as the porous carbon network ensures effective electron transport and favors the transport of lithium ions. The distribution of long-, medium-, and short-chain intermediates at different depth of discharge levels demonstrates that the discharge process proceeds locally at different rates which can be attributed to local differences in the Lithium ion and electron conductivity.

Galvanostatic (re)charge process: During recharge Li_2S undergoes a multi-step reaction to be gradually oxidized back to zerovalent sulfur. The coexistence of Li_2S_x ($x\approx4$) and Li_2S_x ($x\approx6$) from 16 to 88% SOC is evidenced by their corresponding Raman signals. These two representative peaks reach their maximum intensity at $\approx60\%$ SOC and then decay. At the same time, the EsB images at 30% SOC in Figure 5e and Figure S16 (Supporting Information) show predominantly the presence of Li_2S_2/Li_2S. Minor instances of short and medium chain LiPSs can also be observed. It should be noted that Li_2S_2 as a metastable intermediate phase plays a significant role in the initial charging. Due to its instability, differentiating between Li_2S_2 and Li_2S is challenging using alternative characterization methods.[34] According to the working mechanism of the EsB detector, Li_2S appears darker than Li_2S_2 or its decomposition products. Regions of blue pixels in the heat map are likely attributed to Li_2S, while green areas may correspond mainly to Li_2S_2 or a uniform distribution of Li_2S and Li_2S_4 in a 2:1 molar ratio. Therefore, it remains uncertain whether Li_2S can be directly oxidized to Li_2S_4 or if Li_2S_2 forms as an intermediate product. However, the de-lithiation process during charging can still be clearly captured by the EsB technique.

At 60% SOC, Figure 5f and Figure S17 (Supporting Information) show that the majority of Li_2S/Li_2S_2 has transformed into short- and medium-chain LiPS, which is also evidenced by the faint Li^7 NMR peak of Li_2S.[28–33] While, in the range of 30–60% SOC the transformation of Li_2S_2 to Li_2S and from Li_2S_2/Li_2S to Li_2S_x ($x\approx4$) and Li_2S_x ($x\approx6$) still contributes to the capacity. With increasing SOC, bright areas appear again that can be assigned to S-DIB or elemental sulfur as in the section shown in Figure 5g at 90% SOC. Again, there is a match with the corresponding Raman spectra. The figures also show that the distribution of S-DIB inside the porous carbon is largely restored after the charging process is completed and the internal structure of the carbon is preserved. However, in some parts shown in Figure S18f (Supporting Information), the inevitable loss of active material due to the shuttle effect was observed, which explains the capacity decay of as much as 10 percent in the first cycle.

In summary, EsB imaging was used to analyze the lithiation and delithiation processes of S-DIB, providing insights into the distribution of reaction intermediates in a porous carbon structure.

To understand the relationships between the structural properties of the carbon matrix, the distribution of S-DIB within it, and the volume changes during (de)lithiation, EsB images of electrodes were recorded after 200, 300, and 500 cycles, corresponding to 95%, 80%, and 60% capacity retention, respectively. **Figures 6a** and S19 (Supporting Information) show that after 200 cycles, all carbon cells are still filled with S-DIB, and the structure of the carbon matrix remains intact. However, after 300 cycles (Figure 6b; Figure S20, Supporting Information), some empty carbon pores and compressed carbon cells appear. The number of empty carbon cells increases with cycling, and after 500 cycles, several areas show collapsed cellular carbon structures. In comparison to the 200-cycle electrode, the 500-cycle electrode show a slight decrease in brightness. EsB results after long cycling proves potential loss of sulfur and the simultaneous presence of inactivated Li_2S/Li_2S_2 in the electrode.

XPS spectra of the cycled cathodes (Figure 6d) display 5 different peak signatures that can be associated to sulfate, thiosulfate, bridging S, terminal S and S^{2-} at 169.5, 167.6, 164.0, 162.2, and 160.6 eV. Sulfate and thiosulfate originate from sulfur in the electrolyte salt and its decomposition products, bridging sulfur corresponds to sulfur connected to other sulfur atoms in a sulfur chain, while the terminal sulfur peak emerges from sulfur at the end of a sulfur chain. With cycling the integral intensity of the active sulfur species decreases, confirming the loss of active sulfur. After 500 cycles the peak of terminal sulfur increases and a new peak at 160.6 eV and its satellite at 161.8 eV indicate also the presence of Li_2S.[35] The increase of the terminal sulfur peak can be explained by the increased formation of short-chained polysulfides, which are not converted back to elemental sulfur. Together with the presence of Li_2S, this indicates that at 500 cycles more and more inactive sulfur compounds accumulate in the electrode, which could be due to an increase of the electrochemical impedance, affecting the charge transfer process at the HPC-electrolyte interface.

Electrochemical impedance spectroscopy (EIS) was used to study the effect of the deterioration of the carbon host structure during cycling. Data was gathered using a three-electrode setup. Figure S22 (Supporting Information) shows impedance curves of
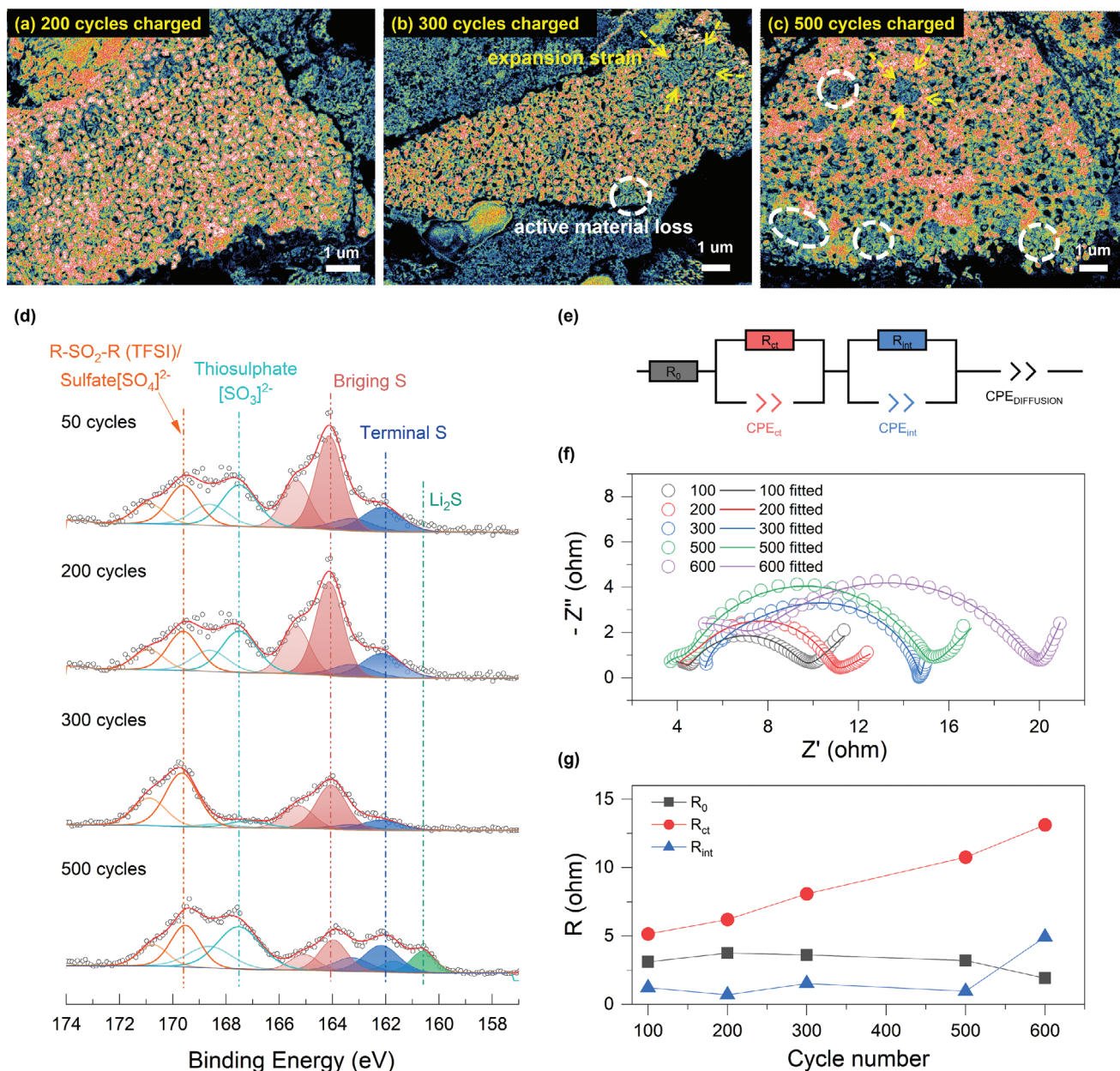
ADVANCED
SCIENCE NEWS

www.advancedsciencenews.com

ADVANCED
ENERGY
MATERIALS

www.advenergymat.de

Figure 6. EsB cross-section view of the charged electrode after a) 200 cycles, b) 300 cycles, and c) 500 cycles. d) XPS of the charged electrode after 50, 200, 300, and 500 cycles. e) The equivalent circuit which was used to fit EIS results. f) EIS profiles and fitting profiles of cycled cathodes. g) The plots of R_0, R_{int}, and R_{ct} as a function of cycle number.

a cycled cathode and anode, with a fresh lithium electrode as the reference. The combined impedance spectra from the anode and cathode against the reference match the spectra from the anode against the cathode, indicating that three-electrode impedance measurements can clarify the contributions of cathode and anode impedance. Figure 6f shows the impedance spectra of sulfur cathodes and anodes after cycling, fitted using the equivalent circuit in Figure 6e.[36–38] The circuit's resistance component (R_n) reflects ohmic resistance. $R_{int}//CPE_{int}$ represents interphase contact resistance and its associated capacitance, simulating electron conduction from the cathode collector to the reaction site.

$R_{ct}//CPE_{dl}$ reflects charge transfer resistance and its associated capacitance. Figure 6g shows plots of R_0, R_{int}, and R_{ct} as a function of cycle number. The trend for R_{ct} indicates its significant role during cycling. With longer cycling, the active mass surface becomes increasingly covered by insulating layers of Li_2S_2/Li_2S. Another factor increasing R_{ct} is HPC degradation, as the charge transfer reaction occurs at the carbon-sulfur-electrolyte interface. As a result, morphological distortions within the cathode matrix reduce the efficiency of interactions with the solid and dissolved sulfur species. Despite continuous degradation, HPC largely retains its role as an electrically conductive scaffold, allowing

extended cycling of the sulfur composite electrode despite evident morphological and structural changes. In conclusion, EsB imaging was used for the first time to reveal lithium sulfide accumulation and carbon scaffold degradation during cycling and a correlation with the electrochemical impedance spectra of the sulfur was established.

To further investigate the effects of chemical and physical confinement on the shuttle effect by DIB and HPC, respectively, EsB images of S@HPC and S-DIB after cycling were analyzed. The images reveal significantly lower sulfur distributed in S@HPC compared to S-DIB@HPC (Figure S23, Supporting Information). The lower amount of sulfur present in the carbon frameworks accounts for its low capacity of only 102 mAh g^{-1} after 500 cycles, indicating that physical confinement by HPC alone is not effective against the shuttle effect. For the S-DIB electrode, direct comparison with S-DIB@HPC is challenging due to less homogenous distribution of S-DIB (Figure S24, Supporting Information). However, the substantial loss of active material before and after cycling highlights the beneficial role of HPC in the composite. XPS characterization of the S-DIB and S@HPC electrodes after cycling in a charged state further supports these findings. As shown in Figure S25 (Supporting Information), the peak of bridging sulfur after cycling in S-DIB@HPC is much more pronounced than in the other two electrodes. The weak bridging peak in S@HPC corresponds to its very low capacity after cycling. Additionally, there is a higher concentration of unoxidized dead Li$_2$S in S@HPC and S-DIB compared to S-DIB@HPC.

3. Conclusion

In summary, we have demonstrated the successful synthesis of S-DIB within a porous, interconnected carbon structure via inverse vulcanization. This novel composite was designed for uniform S-DIB distribution and enhanced electronic and ionic transport to retaining polysulfide species. Consequently, our S-DIB@HPC material maintained a high discharge capacity over 500 cycles, with a capacity loss of only 0.04% per cycle as a sulfur cathode. Additionally, the ordered structure served as an excellent model for studying sulfur species evolution and spatial distribution. We introduced a new EsB-based visualization technique to observe oxidized/reduced sulfur and intermediate stages during de/lithiation within ion-polished electrode cross-sections. These findings discuss the relationship between cyclic degradation and factors such as active material loss, structural distortion, internal stress, and system impedance. The detection of intermediates with an EsB detector offers valuable insights for in-depth studies of sequential reactions and complex processes in sulfur-containing batteries.

4. Experimental Section

Synthesis of HPC, S@HPC, S-DIB, and S-DIB@HPC: HPC was obtained by calcinating tannic acid etched precursors of ZIF-8 at 950 °C as reported in brief.[39] To begin with, 9.35 g of zinc acetate dihydrate was dissolved in 100 ml of deionized water and 28 g of 2-methylimidazole was dissolved in 150 ml of deionized water, respectively. Then the zinc precursor solution was steadily added into the 2-methylimidazole solution. The resulting mixture was stirred for 5 min. After stirring, the mixture was left at room temperature for 24 h. Subsequently, the mixture was then cen-

trifuged and washed three times to ensure thorough cleaning. The ZIF-8 precipitate that resulted from this process was then dried at 80 °C for 12 h to obtain ZIF-8 white powder. 2 g ZIF-8 powder was dispersed into water to achieve a concentration of 0.01 g mL^{-1} for the ZIF-8 suspension. Then 200 g of tannic solution (0.025 g mL^{-1}) was introduced into the ZIF-8 suspension. This mixture was then maintained under stirring for 30 min. After centrifugation and drying, the resultant tannic acid etched ZIF-8 was obtained, which was then directly carbonized at a temperature of 950 °C for 2.5 h under Argon atmosphere. The HPC was finally prepared.

S@HPC was prepared by heating the pre-mixed sulfur powder (70 wt%) and HPC (30 wt%) at 155 °C for 6 h in a well-sealed tube filled with Ar.

For S-DIB, to a 20 mL glass vial equipped with a magnetic stirring bar was added 4.5 g sulfur and heated to 185 °C in an oil bath until a clear yellow molten phase was formed. 0.5 g DIB was then added to the molten sulfur. The reaction mixture was stirred to 15 min until it stopped. This reaction could be visually traced by the complete change of the color from orange to red. The resulting copolymer was cooled down and collected by breaking the glass.

For S-DIB@HPC, the well-mixed HPC and sulfur were sealed in a container and heated at 175 °C for 5 min to conduct the sulfur-melt diffusion procedure. Successively, 10 wt% DIB (in relation to the mass of sulfur) was added and the temperature was increased to 185 °C to promote the efficient initiation of the polymerization. Complete reaction of the medium can be observed within ≈8 min, at which point the reaction mixture was allowed to cool down to ambient temperature to obtain S-DIB@HPC.

DSC Measurement: Differential scanning calorimetry was performed on a 214 Polyma DSC device from NETZSCH (Selb, Germany). Around 5 mg of sample were precisely (Δ = 0.005 mg) weighed in an aluminum pan with a pierced lid for measurement. An aluminum pan filled with air was used as a reference and the heating rate was typically set to 10 K min^{-1} for all measurements.

TGA Measurement: TGA was carried out on an STA 449C Jupiter instrument (NETZSCH, Germany). All TGA measurements were done in argon atmosphere from room temperature to 400 °C with a constant heating rate of 5 K per minute and an argon flow.

Electrochemical Measurement: 75 wt% S-DIB@HPC, S@HPC and 15 wt% Ketjenblack and 10 wt% LA133 (3%) latex were mixed to get a slurry. To ensure the electrodes are comparable, the ratio of S-DIB slurry was 60 wt% S-DIB, 30 wt% Ketjenblack and 10 wt% binder. Then the slurry was coated on Al foils, dried at room temperature overnight and then at 60 °C under vacuum for 6 h. Then the dried electrodes were punched into small disk with a diameter of 12 mm as sulfur cathodes. The areal sulfur loading was ≈1.6 mg S cm^{-2}. Electrochemical measurements were conducted using standard 2025-coin-type cells, where a piece of Li foil with a diameter of 14.0 mm was used as the anode and a piece of Celgard 2500 served as the separator. 1.0 mol L^{-1} LiTFSI and 1 wt % LiNO$_3$ dissolved in DOL/DME (v/v = 1:1) solvents was adopted as the electrolyte. The E/S ratio was 12 μL electrolyte/mg$_{sulfur}$ for regular condition and 8 μL electrolyte/mg$_{sulfur}$ for lean electrolyte condition. The cells were galvanostatically cycled between 1.7–2.7 V on the VMP-3 under different C-rates (1 C = 1675 mA g^{-1}). The capacity was calculated based on the mass of sulfur in the electrode. The CV curves with a potential window of 1.6–2.8 V and EIS (10 mHz–100 kHz) measurements were operated on a Biologic VMP-3 multi-channel workstation. The same instrument was also used to perform galvanostatic intermittent titrations (GITT), by alternating 20 minute's 0.05 C constant current pulses with the open circuit voltage (OCV) periods of 2 h. *Operando* Raman test was conducted using a coin cell with a quartz window.

EsB-Assisted SEM Measurement: In this work, cross-sections of electrodes were prepared using the broad argon ion beam slope-cutting and polishing system, GATAN PECS II. Electrodes were ion-polished by Ar beam under an acceleration of 6 kV for 8 h. The modulation was set to "Single". The whole process was conducted under vacuum or Ar atmosphere to avoid oxidation. The polished electrodes were analyzed in an SEM (Zeiss Gemini2). The ion-polished electrodes were transferred to the SEM chamber using a shuttle tool under the protection of inert gas. the EsB was set to 1500 V = 0.6 Ep (Primary beam energy). Working distance (3.8 mm), beam current (600 pA) and other parameters were kept constant

while capturing the images to avoid their influence on the brightness of the images.

X-Ray Photoelectron Spectroscopy: XPS was performed using a K-Alpha$^+$ instrument (Thermo Fisher Scientific) with a monochromatic Al-Kα X-ray source (1486.6 eV). The sample storage and transportation to the spectrometer for XPS characterization were carried out in an airtight transport vessel under Ar. Thermo Avantage software was used to perform data acquisition and processing as described elsewhere.

Raman Measurement: A LabRAM HR Evolution spectrometer (HORIBA scientific), equipped with a HeNe laser ($\lambda = 632.8$ nm, $E_{laser} = 1.9876$ eV). A 600 grooves mm^{-1} grating along with a 50× magnification (NA = 0.5) objective was employed, resulting in a spot size of ≈2 µm.

NMR Measurement: ^{7}Li magic-angle spinning (MAS) NMR experiments were conducted on a Bruker Avance 200 MHz spectrometer at a magnetic field of 4.7 T. Spectra were acquired at a Larmor frequency of 77.8 MHz with 1.3 mm rotors and spinning at 60 kHz. A rotor-synchronized Hahn-echo pulse sequence (90°-τ-180°-τ-acquisition) was used with a 90° pulse length of 0.9 µs and a recycle delay of 1 s. The ^{7}Li NMR shifts were referenced using an aqueous 1 M LiCl solution (0 ppm). All spectra were normalized with respect to sample mass and number of scans.

Pore Size Distribution Measurement: The N$_2$ adsorption/desorption isotherms were measured at 77 K with a Micromeritics ASAP 2020 instrument. The pore size distribution for micropores and mesopores was analyzed using the Horvath–Kawazoe (HK) and Barrett–Joyner–Halenda (BJH) models.

Supporting Information

Supporting Information is available from the Wiley Online Library or from the author.

Conflict of Interest

The authors declare no conflict of interest.

Data Availability Statement

The data that support the findings of this study are available from the corresponding author upon reasonable request.

[1] G. Zhou, H. Chen, Y. Cui, *Nat. Energy.* **2022**, *7*, 312.

[2] L. Hou, X. Zhang, N. Yao, X. Chen, B. Li, P. Shi, C. Jin, J. Huang, Q. Zhang, *Chem* **2022**, *8*, 1083.

[3] C.-H. Chang, A. Manthiram, *ACS Energy Lett.* **2017**, *3*, 72.

[4] W. J. Chung, J. J. Griebel, E. T. Kim, H. Yoon, A. G. Simmonds, H. J. Ji, P. T. Dirlam, R. S. Glass, J. J. Wie, N. A. Nguyen, B. W. Guralnick, J. Park, A. Somogyi, P. Theato, M. E. Mackay, Y. E. Sung, K. Char, J. Pyun, *Nat. Chem.* **2013**, *5*, 518.

[5] H. Kim, J. Lee, H. Ahn, O. Kim, M. J. Park, *Nat. Commun.* **2015**, *6*, 7278.

[6] H. Kang, H. Kim, M. J. Park, *Adv. Energy Mater.* **2018**, *8*, 1802423.

[7] Q. Zeng, X. Li, W. Gong, S. Guo, Y. Ouyang, D. Li, Y. Xiao, C. Tan, L. Xie, H. Lu, Q. Zhang, S. Huang, *Adv. Energy Mater.* **2022**, *12*, 2104074.

[8] J. Park, E. T. Kim, C. Kim, J. Pyun, H.-S. Jang, J. Shin, J. W. Choi, K. Char, Y.-E. Sung, *Adv. Energy Mater.* **2017**, *7*, 1700074.

[9] G. Hu, Z. Sun, C. Shi, R. Fang, J. Chen, P. Hou, C. Liu, H.-M. Cheng, F. Li, *Adv. Mater.* **2017**, *29*, 1603835.

[10] K. Shen, H. Mei, B. Li, J. Ding, S. Yang, *Adv. Energy Mater.* **2018**, *8*, 1701527.

[11] R. Du, Y. Wu, Y. Yang, T. Zhai, T. Zhou, Q. Shang, L. Zhu, C. Shang, Z. Guo, *Adv. Energy Mater.* **2021**, *11*, 2100154.

[12] Y. Yan, C. Cheng, L. Zhang, Y. Li, J. Lu, *Adv. Energy Mater.* **2019**, *9*, 1900148.

[13] S.-H. Yu, X. Huang, K. Schwarz, R. Huang, T. A. Arias, J. D. Brock, H. D. Abruña, *Energy Environ. Sci.* **2018**, *11*, 202.

[14] M. Sadd, S. De Angelis, S. Colding-Jørgensen, D. Blanchard, R. E. Johnsen, S. Sanna, E. Borisova, A. Matic, J. R. Bowen, *Adv. Energy Mater.* **2022**, *12*, 2103126.

[15] M. Li, W. Liu, D. Luo, Z. Chen, K. Amine, J. Lu, *ACS Energy Lett.* **2022**, *7*, 577.

[16] C. Geng, W. Hua, D. Wang, G. Ling, C. Zhang, Q. H. Yang, *SusMat* **2021**, *1*, 51.

[17] W. Xu, S. Lang, K. Wang, R. Zeng, H. Li, X. Feng, M. R. Krumov, S.-M. Bak, C. J. Pollock, J. Yeo, Y. Du, H. D. Abruña, *Sci. Adv.* **2023**, *9*, eadi5108.

[18] S. Lang, S.-H. Yu, X. Feng, M. R. Krumov, H. D. Abruña, *Nat. Commun.* **2022**, *13*, 4811.

[19] C. Wei, Y. Wang, Y. Zhang, L. Tan, Y. Qian, Y. Tao, S. Xiong, J. Feng, *Nano Res.* **2021**, *14*, 3576.

[20] Y. X. Yao, X. Q. Zhang, B. Q. Li, C. Yan, P. Y. Chen, J. Q. Huang, Q. Zhang, *InfoMat* **2019**, *2*, 379.

[21] C. Abetz, P. Georgopanos, C. Pistidda, T. Klassen, V. Abetz, *Adv. Mater. Technol.* **2022**, *7*, 2101584.

[22] E. Homede, M. Abo Jabal, O. Manor, *Adv. Funct. Mater.* **2020**, *30*, 2005486.

[23] R. Podor, J. Mendonça, J. Lautru, H. P. Brau, D. Nogues, A. Candeias, P. Horodysky, A. Kolouch, M. Barreau, X. Carrier, N. Ramenatte, S. Mathieu, M. Vilasi, *J. Microsc.* **2021**, *282*, 45.

[24] J. Heiner, In EMC 2008 14th European Microscopy Congress, Springer, Aachen, Germany **2008**.

[25] L. Li, J. S. Nam, M. S. Kim, Y. Wang, S. Jiang, H. Hou, I. D. Kim, *Adv. Energy Mater.* **2023**, *13*, 2302139.

[26] T. Zhang, F. Hu, W. Shao, S. Liu, H. Peng, Z. Song, C. Song, N. Li, X. Jian, *ACS Nano* **2021**, *15*, 15027.

[27] S. H. Je, T. H. Hwang, S. N. Talapaneni, O. Buyukcakir, H. J. Kim, J.-S. Yu, S.-G. Woo, M. C. Jang, B. K. Son, A. Coskun, J. W. Choi, *ACS Energy Lett.* **2016**, *1*, 566.

[28] P. Chen, Z. Wu, T. Guo, Y. Zhou, M. Liu, X. Xia, J. Sun, L. Lu, X. Ouyang, X. Wang, Y. Fu, J. Zhu, *Adv. Mater.* **2021**, *33*, 2007549.

[29] A. Garitagoitia Cid, R. Rosenkranz, E. Zschech, *Adv. Eng. Mater.* **2016**, *18*, 185.

[30] Z. Wang, Y. Li, H. Ji, J. Zhou, T. Qian, C. Yan, *Adv. Mater.* **2022**, *34*, 2203699.

ADVANCED
SCIENCE NEWS

www.advancedsciencenews.com

ADVANCED
ENERGY
MATERIALS

www.advenergymat.de

[31] W. Yao, C. Tian, C. Yang, J. Xu, Y. Meng, I. Manke, N. Chen, Z. Wu, L. Zhan, Y. Wang, R. Chen, *Adv. Mater.* **2022**, *34*, 2106370.

[32] A. Hoefling, D. T. Nguyen, P. Partovi-Azar, D. Sebastiani, P. Theato, S.-W. Song, Y. J. Lee, *Chem. Mater.* **2018**, *30*, 2915.

[33] M. U. M. Patel, I. Arčon, G. Aquilanti, L. Stievano, G. Mali, R. Dominko, *ChemPhysChem* **2014**, *15*, 894.

[34] S. Zhou, J. Shi, S. Liu, G. Li, F. Pei, Y. Chen, J. Deng, Q. Zheng, J. Li, C. Zhao, I. Hwang, C.-J. Sun, Y. Liu, Y. Deng, L. Huang, Y. Qiao, G.-L. Xu, J.-F. Chen, K. Amine, S.-G. Sun, H.-G. Liao, *Nature* **2023**, *621*, 75.

[35] Y. Zhang, J. Liu, J. Wang, Y. Zhao, D. Luo, A. Yu, X. Wang, Z. Chen, *Angew. Chem., Int. Ed.* **2021**, *60*, 26622.

[36] N. Ogihara, S. Kawauchi, C. Okuda, Y. Itou, Y. Takeuchi, Y. Ukyo, *J. Electrochem. Soc.* **2012**, *159*, A1034.

[37] S. Waluś, C. Barchasz, R. Bouchet, F. Alloin, *Electrochim. Acta.* **2020**, *359*, 136944.

[38] N. A. Cañas, K. Hirose, B. Pascucci, N. Wagner, K. A. Friedrich, R. Hiesgen, *Electrochim. Acta.* **2013**, *97*, 42.

[39] M. Kim, R. Xin, J. Earnshaw, J. Tang, J. P. Hill, A. Ashok, A. K. Nanjundan, J. Kim, C. Young, Y. Sugahara, J. Na, Y. Yamauchi, *Nat. Protoc.* **2022**, *17*, 2990.

2402996 (12 of 12)